PHYSICAL REVIEW A **101**, 053421 (2020)

Quantum path interferences and selection in interband solid high-order harmonic generation in MgO crystals

Tian-Jiao Shao,[1,2] Ling-Jie Lü,[1,2] Jia-Qi Liu,[1,2] and Xue-Bin Bian[1,*]

[1]*State Key Laboratory of Magnetic Resonance and Atomic and Molecular Physics, Wuhan Institute of Physics and Mathematics, Innovation Academy for Precision Measurement Science and Technology, Chinese Academy of Sciences, Wuhan 430071, China*

[2]*School of Physical Sciences, University of Chinese Academy of Sciences, Beijing 100049, China*

(Received 15 November 2019; accepted 17 April 2020; published 12 May 2020)

We theoretically investigate the quantum path interferences in interband transitions in solid high-order harmonic generation. The field strength scaling of the 19th harmonic yield from MgO crystal driven by 1600-nm lasers exhibits a sharp minimum. By solving the semiconductor Bloch equation, we separate the short and long trajectories. Our numerical calculation shows that this minimum originates from the coherent interferences between the short and long trajectories. We also illustrate that the interference minimum depends sensitively on the band dispersion, which can be used to retrieve the band structure accurately. We further report that the two-color fields can select the short or long quantum path effectively by controlling the phase. The yield at the plateau or cutoff region of the harmonic spectra can be enhanced by around one order of magnitude by adding a third harmonic with an intensity of only 10% of the fundamental field. Moreover, an isolated attosecond pulse (IAP) is synthesized by controlling the harmonic trajectories in the two-color scheme. The yield of this IAP is enhanced by one order of magnitude compared with the IAP generated by the single-color scheme.

DOI: 10.1103/PhysRevA.101.053421

I. INTRODUCTION

The atomic and molecular high-order harmonic generation (HHG) [1–3] has been intensively investigated for synthesizing the isolated attosecond pulse (IAP) [4,5], imaging the electronic distribution [6–8] and molecular structure [9,10], and probing intramolecular dynamics [11,12] with attosecond resolution. The atomic HHG spectra are characterized by a harmonic frequency comb structure [1]. It covers an energy range of several hundred eV with a sharp cutoff [2,3]. The scheme of the atomic and molecular HHG has been described by the well-known three-step model [2]: outer-shell electrons are freed by the laser field through tunnel ionization, then they are accelerated, and then they recombine with the ions and emit attosecond x-ray photons. For one harmonic, there are long, short, and multiple-return trajectories determined by their traveling time in the process.

The solid harmonic spectra have been experimentally observed in ZnSe [13]. In 2011, the nonperturbative solid high-order harmonic generation in wurtzite ZnO crystal was experimentally measured [14]. Recently, solid HHG has become a heated issue [13,14,14–16,16–37]. It has many characteristics different from the atomic HHG, such as the double-plateau structure [16,17], different dependence on the ellipticity of the driving field [18,19], linear dependence of the cutoff energy as a function of the driving laser field strength [16,21], and so forth. Driven by the multicycle lasers, solid HHG spectra also have harmonic frequency combs [20,21] like the atomic HHG spectra. They also emit photons covering a wide range of energy with a cutoff. For solid HHG, a three-step model is also proposed theoretically to explain the interband transition [21,22]: (1) driven by strong lasers, the electron-hole pairs are generated; (2) the electrons and holes are accelerated by the oscillating laser field; and (3) the harmonic photons are emitted when the electrons and holes recombine. The gauge dependence of inter- and intraband harmonics has been discussed in Refs. [23,24]. In Refs. [25,26], the inter- and intraband currents should be gauge independent by properly defining the operator.

The solid HHG is promising to be developed as a compact light source [27] since the crystal as HHG target is naturally orientated and has a high density. The solid HHG spectra also include information such as the electronic band structure of the solid target [28], bond information [29], the crystal spatial symmetry and laser temporal symmetry [30,31,38], and so on.

The HHG spectra also include temporal information of the electron dynamics [39–42]. Since the electron wave packet accumulates phases when it is driven by laser pulses after ionization, the temporal information such as the chirp of electron trajectories will be mapped into the fringe patterns of the spectra [41].

The quantum path interference in atomic HHG has been already investigated [39–42]. The long trajectory contribution and its interference with the short one have been experimentally confirmed [39] and theoretically investigated [40]. The quantum path interference in solid HHG from sapphire has been confirmed recently [43]. It enables the measurement of electron dynamics and control of the harmonic emission properties on the ultrafast time scale [43]. It will benefit us to analyze the structural and dynamic information recorded in the spectra. Moreover, through controlling the interference,

---

[*] xuebin.bian@wipm.ac.cn

the harmonic emission in solid HHG is allowed to be selectively suppressed or enhanced [43].

The interference phenomena in molecular HHG have been observed, such as intramolecular interference during the recombination process [9], interference between different molecule orbits [44,45], and so on. Interference in solid HHG has been investigated and discussed theoretically recently, which includes the following.

(i) Inter- and intraband current interference [25]: The destructive interference between interband and intraband transitions leads to the suppression of some harmonics. The prerequisite for this type of interference requires that the intensities of interband and intraband transitions are comparable.

(ii) Subcycle interference [33]: The electrons pumped to the conduction band in different laser subcycles may interfere with each other. This interference covers the entire interband harmonic spectrum.

(iii) Multiband interference [15,34]: The recombination of electrons and holes from different bands may interfere with each other.

(iv) Multielectron intraband interference [46]: The emissions from different k points interfere with each other when the intraband current dominates.

(v) Interference of HHG from different sites: Mrudul *et al.* reported another type of interference due to real-space recollision caused by the periodic lattice cell [47], which is similar to intramolecular interference. The position of this interference minimum is independent of the depth of the periodic potential and driving laser intensity; however, it is sensitively dependent on the lattice constant.

The solid HHG is very sensitive to the band structure. In this paper, we investigate the short and long quantum path interference in interband transitions in MgO crystal theoretically, which is different from the interferences mentioned above. The field strength scaling of the 19th harmonic yield in MgO crystal driven by a multicycle 1600-nm laser field along the ΓX direction exhibits a sharp minimum. On the basis of the semiconductor Bloch equation (SBE) [48–50] and the Keldysh approximation [51], a semianalytical solution of the interband current is obtained [21,48], which allows the short and long trajectory contributions to be separated [43,52]. Our calculation confirms the interference between the short and long trajectories in interband transitions, which can be further used as a sensitive tool to retrieve the band structure.

Next, our calculation shows the quantum path selection in solid HHG by the two-color fields [53] synthesized by a multicycle fundamental pulse and its third harmonic. We find that a proper relative phase can shift the tunneling gating to the conduction band, which enables the selection of only short or only long quantum paths in interband transitions. Through choosing a proper relative phase, the solid HHG intensity is enhanced by one order of magnitude by the two-color field. Moreover, a single harmonic emission burst is selected by using the two-cycle fields.

II. THEORETICAL METHOD

Semiconductor Bloch equation

In this paper, the solid HHG simulation is performed by solving the one-dimensional SBE, which can be expressed by [21,48]

$$\dot{\pi}(K,t) = -\frac{1}{T_2}\pi(K,t) - i\Omega(K,t)w(K,t)e^{-iS(K,t)}, \tag{1}$$

$$\dot{n}_b(K,t) = is_b\Omega^*(K,t)\pi(K,t)e^{iS(K,t)} + \text{c.c.}, \tag{2}$$

where $\pi(K,t)$ is the polarization strength between the conduction band (CB) and the valence band (VB). $E(t)$ is the electric field of the laser, and $\Omega(K,t) = d(K,t)E(t)$ is the Rabi frequency. $d(k)$ is the transition dipole moment (TDM). The MgO has cubic crystal structure and belongs to the $Fm\bar{3}m$ space group. At the Γ point, the TDM d_0 equals to 4.0593, which is evaluated from the density-functional theory (DFT) calculation [29]. The details can be found in Appendix A. Its k dependence can be calculated by the first-order $\mathbf{k}\cdot\mathbf{p}$ theory [49,50]. Since the $\mathbf{k}\cdot\mathbf{p}$ theory as a perturbation theory is not accurate enough for the k points far from the Γ point, in this paper, unless specifically mentioned, we use the TDM from DFT calculations, which are discussed in detail in the Appendices. Since the electron dynamics along the Γ-X direction is inversion symmetric with respect to the Γ point, both the phase of the TDM and the Berry connection are ignored in this paper [54,55]. $w(K,t) = n_C(K,t) - n_V(K,t)$ is the population difference between the CB and VB, and $s_b = -1, 1$ stands for the VB and CB, respectively. $S(K,t) = \int_{-\infty}^{t} \varepsilon_g[K + A(t')]dt'$ is defined as the classical action, which is independent of the TDM. T_2 is a dephasing-time term describing the coherence between the electron and hole.

The intraband currents along the valence and conduction bands can be written as follows:

$$j_{\text{intra}}(t) = \sum_{m=c,v} \int_{\text{BZ}} v_m[K + A(t)]n_m(K,t)d^3K, \tag{3}$$

where $v_m(K) = \nabla_k E_m(K)$ and $n_m(K,t)$ are the group velocity and population in band m, respectively. v_m is strongly related to the band structure. $m = v$ is for the valence band and $m = c$ is for the conduction band, respectively. The interband currents can be written as

$$j_{\text{inter}}(t) = \frac{d}{dt}\int_{\text{BZ}} p[K + A(t)]d^3K, \tag{4}$$

where $p[K + A(t)] = d[K + A(t)]\pi[K + A(t)]e^{iS(K,t)} + \text{c.c.}$ is the interband polarization, which is strongly dependent on the transition dipole between the CB and VB. The inter- and intraband harmonics are calculated by the Fourier transform of the interband current $|\mathcal{F}[j_{\text{inter}}(t)]|^2$ and intraband current $|\mathcal{F}[j_{\text{intra}}(t)]|^2$, respectively.

The total currents contributed by both interband and intraband transitions are $j_{\text{tot}}(t) = j_{\text{inter}}(t) + j_{\text{intra}}(t)$. The total HHG spectra are then given by Fourier transform of the total current, $|\mathcal{F}[j_{\text{total}}(t)]|^2$.

On the basis of the Keldysh approximation [$w(t) = n_v(t) - n_c(t) \approx 1$], Eqs. (1) and (2) can be decoupled. In this way, the interband transition in Eq. (4) can be integrated as [21,48]

$$\mathbf{j}_{\text{inter}}(\omega) = \omega \int_{\text{BZ}} d^3k d(k) \int_{-\infty}^{\infty} dt e^{-i\omega t} \int_{-\infty}^{t} dt' E(t') d^*(k_{t'}) \times e^{-iS(k,t',t)-(t-t')/T_2} + \text{c.c.} \tag{5}$$

To separate the short and long trajectories in interband transitions, we insert a filter function $F(t-t')$ to select the trajectories [43,52]:

$$\mathbf{j}_{\text{inter}}(\omega) = \omega \int_{\text{BZ}} d^3k\mathbf{d}(k) \int_{-\infty}^{\infty} dt e^{-i\omega t} \int_{-\infty}^{t} dt' E(t')\mathbf{d}^*(k_{t'}) \times e^{-iS(k,t',t)-(t-t')/T_2} F(t-t') + \text{c.c.} \tag{6}$$

In order to select the short trajectory contribution, we set $F(t-t') = 1$ for $t-t' < 0.65T_0$ and $F(t-t') = 0$ for $t-t' > 0.65T_0$. For the long trajectory, we set $F(t-t') = 0$ for $t-t' < 0.65T_0$ and $F(t'-t) = 1$ for $0.65T_0 < t-t' < T_0$, where T_0 is an optical cycle (o.c.) of the driving field and $0.65T_0$ is the excursion time for the cutoff trajectories of the excited electrons in the CB obtained by the saddle-point approximation [21,48].

III. RESULTS AND DISCUSSIONS

A. Short and long trajectory interference in interband transitions

In this paper, the expression of the monochromatic laser field can be written as

$$E(t) = E_0 \exp\left[-2\ln(2)t^2/\tau_0^2\right]\cos(\omega t + \varphi_{\text{CE}}), \tag{7}$$

where ω is the frequency of the laser field, E_0 is the field strength, the envelope is approximated as a Gaussian shape, τ_0 is the full width at half maximum (FWHM) of the temporal profile, and $\varphi_{\text{CE}} = 0$ is the carrier-envelope phase (CEP).

The two-color synthesized laser field can be expressed as

$$E_{\text{total}}(t) = E_1 \exp\left[-2\ln(2)t^2/\tau_1^2\right]\cos(\omega_1 t) + E_2 \exp\left[-2\ln(2)(t+t_0)^2/\tau_2^2\right]\cos[\omega_2(t+t_0)], \tag{8}$$

where E_{total}(t) is the temporal field strength of the two-color field. E_1 and E_2 are the field strengths of the fundamental pulse and control pulse, respectively. Both the CEP φ_{CE} of the fundamental pulse and the control field are set to be zero. $\varphi_r = \omega_2 t_0$ is the relative phase and t_0 is the time delay between the two fields. Figure 1(a) shows the recollision energy of the electrons and holes as a function of the tunneling and recombination times, which are calculated through the saddle-point approximation of the SBE [48]. For the monochromatic field, the laser parameters are $\tau_0 = 53.33$ fs (10.0 o.c.), 1600-nm pulse, field strength $E_0 = 0.0059$ a.u. For the tunneling time-dependence curve (olive circles), the long and short trajectories are born before and after the cutoff trajectories, respectively. For the recombination time-dependence curve (magenta diamonds), the short and long trajectories recombine before and after the cutoff trajectories, respectively.

The green solid line shows the temporal driving laser waveform in one cycle. Both the short and long trajectories are generated after the laser peak. Compared with the short trajectory, the chirp of the long trajectory is much smaller. This indicates that, if the long trajectory can be filtered out, the generated harmonic profile can be used to synthesize very short isolated attosecond bursts.

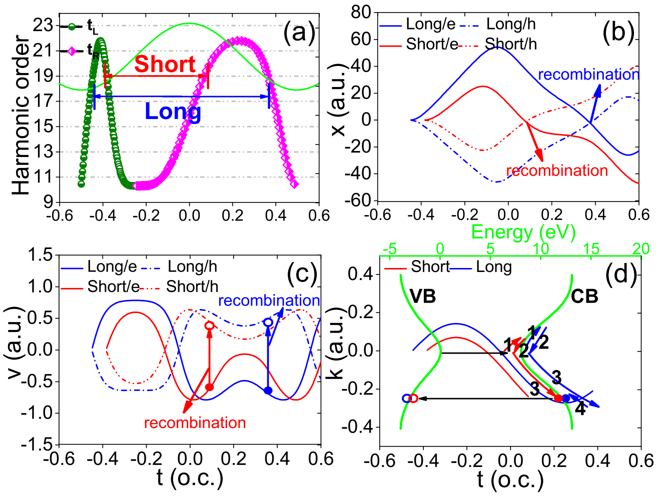

FIG. 1. Long and short trajectories in interband HHG. (a) The recollision energy varies with tunneling (olive circles) and recombination times (magenta diamonds). The green-solid line shows the temporal laser waveform. (b) The displacement of the short trajectories of the electron (red solid line) and hole (red dash-dotted line), and long trajectories of the electron (blue solid line) and hole (blue dashed line) for the 19th harmonic in real space. (c) Same as (b) but for the velocity of the electrons and holes. (d) The temporal crystal momenta of short (red solid line) and long trajectories (blue solid line) of the 19th harmonic in k space; CB and VB are plotted to illustrate the recombination process. Laser parameters: τ_0=53.33 fs (10.0 o.c.), 1600-nm pulse, field strength E_0=0.0059 a.u.

Figure 1(b) presents the short and long trajectories of the 19th harmonic in the real coordinate space. Different from the atomic HHG, both the electrons and holes move, and the recombination time of the electron and hole is determined by the cross point of the trajectory curves of the electron and hole.

Figure 1(c) illustrates the velocity of the electrons and holes contributing to the 19th harmonic. The electrons (holes) along the short and long trajectories both have positive (negative) velocities. Due to the change of direction of the driving field, the velocity of the electrons (holes) of both the short and long trajectories changes. After that, the short trajectory first recombines, and later the long trajectory recombines.

Figure 1(d) demonstrates the time-dependent crystal momentum of the short (red solid line) and long trajectories (blue solid line) of the 19th harmonic in the k space. Both trajectories are generated at the Γ point, and the time-dependent crystal momentum is given by $k(t) = A(t_i) - A(t)$, where t_i is the born time of the electrons and holes, respectively. $A(t)$ is the vector potential of the laser pulse. First, both the short and long trajectories move to the positive crystal momentum direction $(+k)$ as shown in Fig. 1(d). Due to the change of the direction of the laser field in each half cycle, the electron moves back towards the Γ point. Then, the electron moves to the negative crystal momentum $(-k)$. Compared with the short trajectory, the long trajectory moves further to larger positive crystal momentum, then changes direction and moves again towards the Γ point. The electrons and holes of both the short and long trajectories recombine at the same place in the k space. At the band gap equal to the 19th harmonic energy, the electron and hole recombine, and the 19th harmonic photon is emitted. However, the long trajectories move a larger portion of the energy band than the short ones.

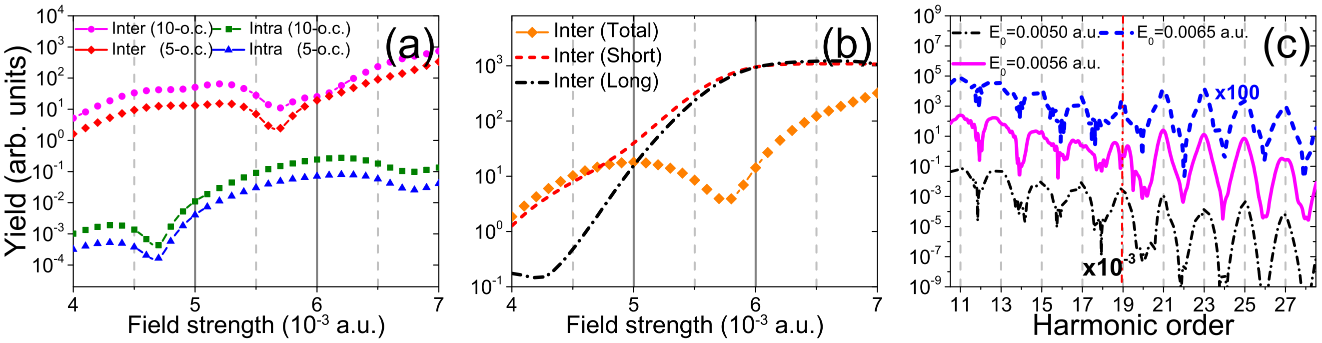

FIG. 2. (a) The 19th harmonic yield vs the driving field strength calculated by the SBE. The interband and intraband transitions driven by the 10- and 5-o.c. laser pulses are compared. (b) The field strength dependence curve of the 19th harmonic contributed by the short (red dashed line) and long trajectory (black dash-dotted line), and total contributions (orange diamond line), driven by 5-o.c. laser pulses. In (a) and (b), the intensity of the 19th harmonic is integrated from $18.8\omega_0$ to $19.2\omega_0$. (c) The solid HHG spectra driven by the 10-o.c. laser field under E_0=0.0050 a.u. (black dash-dotted line), E_0=0.0056 a.u. (magenta solid line), and E_0=0.0065 a.u. (blue dashed line). When the driving field strength E_0=0.0056 a.u., the 19th harmonic shows a clearly splitting minimum pattern instead of a harmonic peak. For comparison, the black dash-dotted line is minimized by a factor of 1000, while the blue dashed line is magnified by a factor of 100. In all the calculations, the dephasing time T_2=0.5 o.c. (2.67 fs for the 1600-nm laser).

The short and long trajectories have different tunneling time, recombination time, and propagation time when they move along an energy band. Thus, the short and long trajectories have accumulated different phases, leading to the destructive interference. Moreover, the accumulated phases of the quantum paths record the information of the energy band. The band structure can be retrieved by measuring the interference fringe patterns.

Figure 2(a) shows the field strength dependence curve of the 19th harmonic calculated by the SBE by using Eqs. (1) and (2). The 19th interband harmonic signal (magenta circle line) driven by a 10-o.c. laser increases as a function of the field strength initially. However, around $E_0 = 0.0058$ a.u., the curve exhibits a sharp minimum. Since the excitation rates depend exponentially on the field strength [51], it is expected that harmonic yields should also depend exponentially on the field strength continuously before saturation. This sudden sharp minimum on the field strength dependence curve indicates that some destructive interference occurs.

The interband harmonic yields (magenta circle line) at all field strengths show a much larger yield than the intraband transition (olive square line). This indicates that the total harmonic spectra are mainly determined by the interband transition, and the intraband contribution can be ignored. The recollision feature in Ref. [29] also suggests that the interband transitions dominate. The 19th interband (red diamond line) and intraband (blue triangle line) harmonic signals driven by a 5-o.c. laser show a similar trend with the 10-o.c. laser, which suggests that the minimum comes from subcycle dynamics.

In Fig. 2(b), we use a semianalytical solution of the interband transition from Eqs. (5) and (6), and the short trajectory contribution, long trajectory contribution, and total interband transition are calculated, respectively. The sharp minimum at E_0=0.0058 a.u. disappears in the field strength dependence curve, which only includes the short or long trajectory contribution. However, this minimum is observed from the semianalytical solution of the total interband transition, which equals to the coherent sum of the short and long trajectory contributions (orange diamonds). This proves that this destructive interference comes from the coherent interference between the short and long trajectories.

Figure 2(c) plots the HHG spectra from the SBE at E_0=0.0056 a.u. (magenta solid line) driven by a 10-o.c. 1600-nm laser pulse. The 19th harmonic shows a sharp splitting minimum instead of the harmonic peak signal, compared with the HHG spectra driven by E_0=0.0050 a.u. (black dash-dotted line) and E_0=0.0065 a.u. (blue dashed line). Moreover, from the HHG spectra driven by E_0=0.0056 a.u., only the 19th harmonic shows this destructive interference minimum. All the other odd harmonics, such as the 15th, 17th, 21st, 23rd, and 25th, still show the harmonic peak structures. In Figs. 2(b) and 2(c), the field strength dependence curve indicates that the interference can be modulated by the driving field strength. Since a pair of short and long trajectories is generated in each half optical cycle, the timescale of the quantum paths is naturally within a half optical cycle. By controlling the field strength, both the short and long quantum paths are modulated on the subfemtosecond timescale.

B. Band-structure retrievement

In this paper, we show that the quantum path interference minimum in HHG spectra can be used to characterize the energy-band dispersion.

The band structure from DFT is taken as the target band to be retrieved. The best choice for the functional expression of the trial band is taken as the natural functional form of the band dispersion [28]. The following function is taken as the trial band formula in our paper: $\epsilon_g(k) = \epsilon_g - (\epsilon_g/2)^{2B} + [(\epsilon_g/2)^2 + (Aa_xk)^2]^B$. This function has a power function part which is able to describe the nonlinearity of the energy dispersion. Only two unknown dispersion parameters A and B need to be determined. This function can be chosen as a rough approximation for the initial guess of the target band.

In our calculations, for example, the parameter B is supposed to be 0.3409. Figure 3(a) shows seven trial values of A

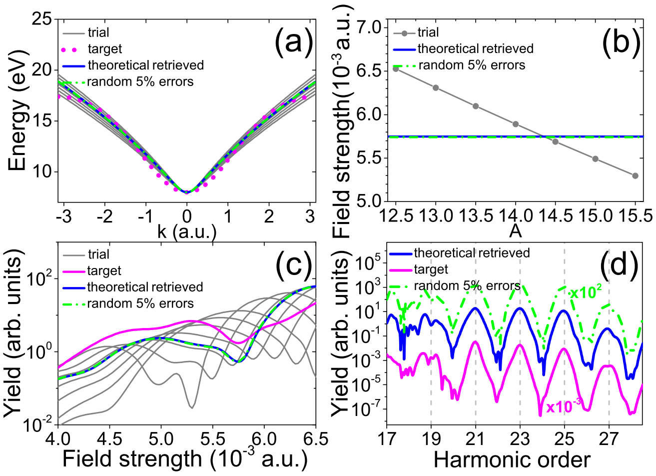

FIG. 3. The energy dispersion of the trial bands (gray solid lines), theoretically retrieved band (blue solid line), retrieved band by assuming random 5% errors in harmonic intensity (green dot-dashed line), and target band (magenta dash-dotted line). (b) The field strength dependent interference minimum vs dispersion parameter A. (c) The field strength dependence curve of the trial bands (gray solid line), theoretically retrieved band (blue solid line), random 5% errors (green dot-dashed line), and target band (magenta circle line). (d) The interband HHG spectra for the theoretically retrieved band (blue solid line), random 5% errors (green dot-dashed line), and target band (magenta solid line) for field strength E_0=0.0057 a.u. Laser parameters: τ_0=26.67 fs (5.0 o.c.), 1600-nm monochromatic pulse, E_0 scales from 0.004 to 0.0065 a.u.

from the 20 guesses. Figure 3(a) shows the band dispersion of the trial bands (B=0.3409, A is varied from 12.50 to 15.50 with a step of 0.5, gray solid line), the target band (magenta dash-dotted line), and the best-retrieved trial band (blue solid line). Figure 3(c) shows the field strength dependence curve of the 19th harmonic for the trial and target bands. By varying the dispersion parameters A, the position of the sharp minimum also varies.

In Fig. 3(b), the gray circles show the destructive interference minimum of each trial band in Fig. 3(c). When A equals 14.358 (blue solid line), the position of the interference minimum of the trial band agrees well with the target band.

In Fig. 3(d), the blue solid line and green dash-dotted line show the harmonic spectra for the theoretical best trial band (A = 14.358) and the case assuming random 5% errors (A=14.373) when the field strength E_0 = 0.0057 a.u. The spectrum for the trial band accords well with the spectrum from the target band (magenta solid line).

Our calculation indicates that the interference minimum is sensitively dependent on the energy dispersion relation. The electron-hole pairs accumulate phases when they move in the energy band. The accumulated phases of the short and long trajectories in the interband transition record the band dispersion information. The quantum path interference minimum provides a possibility for retrieving the band structure of solids. We only include one valence band and one conduction band in our calculation; if more bands contribute to the HHG, this method should not be applicable.

C. Quantum path selection in interband high-order harmonic generation

In atomic HHG, the quantum path selection based on tunnel ionization gating is theoretically proposed [56–58] and observed experimentally [58]. The quantum path selection relaxes the requirement for the duration of the driving field for synthesizing the IAP and provides the possibility for generating a much shorter and brighter attosecond burst. In the following, our calculation reports the quantum path selection of the interband transition in solid HHG by modulating the relative phase of the two-color fields. In our simulation, a 54.17-fs (5-o.c.) E_0 = 0.004-a.u. 3250-nm field is the monochromatic field for driving HHG. The two-color field is composed by a 54.17-fs (5-o.c.) E_1=0.003-a.u. 3250-nm laser as the fundamental pulse, and another 54.17-fs E_2 = 0.001-a.u. 1083.3-nm field (third harmonic) is chosen as the control pulse. We chose these laser parameters since they are all available in today's ultrafast laser technology.

In Fig. 4, the left, middle, and right columns show the solid HHG driven by monochromatic two-color fields with a relative phase of π rad and zero phase shift, respectively. Figures 4(a)–4(c) show the recollision energy of the electrons and holes, temporal electric-field waveforms, and Keldysh excitation rates varying with the tunneling time. Figures 4(d)–4(f) show the temporal harmonic emission by performing a wavelet transform of the total harmonic spectra calculated by the SBE, and the TDM is obtained from $\mathbf{k} \cdot \mathbf{p}$ theory. The laser parameters in simulations are the same as the saddle-point analysis in the upper row. Figures 4(g)–4(i) show temporal harmonic emission similar to the middle row; however, the TDM is obtained from DFT. One may find that the dipole plays a very important role in the relative strength of harmonics. The relative contribution from long and short trajectories changes little as discussed below.

In Figs. 4(a), 4(d), and 4(g), the harmonics are generated by a single-color 54.17-fs (5.0-o.c.) 3250-nm pulse. The long trajectory is generated after the laser peak, and the short trajectory is born later than the long one. Thus, the excitation peak is very near the birth time of the long trajectory. This explains why in the temporal harmonic profile shown in Figs. 4(d) and 4(g) the long trajectory shows a slightly larger yield than the short one.

In Figs. 4(b), 4(e), and 4(h), the harmonics are produced by the 54.17-fs 3250-nm fundamental pulse superposed by its third harmonic with the relative phase of 1.0π rad. In Fig. 4(b), the excitation peak is located slightly after the cutoff trajectory; this indicates that the short trajectories are born with large excitation yield, while the long trajectories are weak. In Figs. 4(e) and 4(h), the temporal harmonic profile simulated by the SBE shows that the short trajectories dominate the temporal harmonic emission.

In Figs. 4(c), 4(f), and 4(i), the system is driven by the same main and control pulse as shown in the middle column but with a zero relative phase shift. In Fig. 4(c), the excitation peak is located at the long trajectory. This indicates that the long trajectories are born with larger excitation yield than the short ones. In Figs. 4(f) and 4(i), the temporal harmonic profile from the SBE illustrates that the long trajectories dominate. Thus, the short or long quantum path can be selected by shifting the relative phase of the two-color fields.

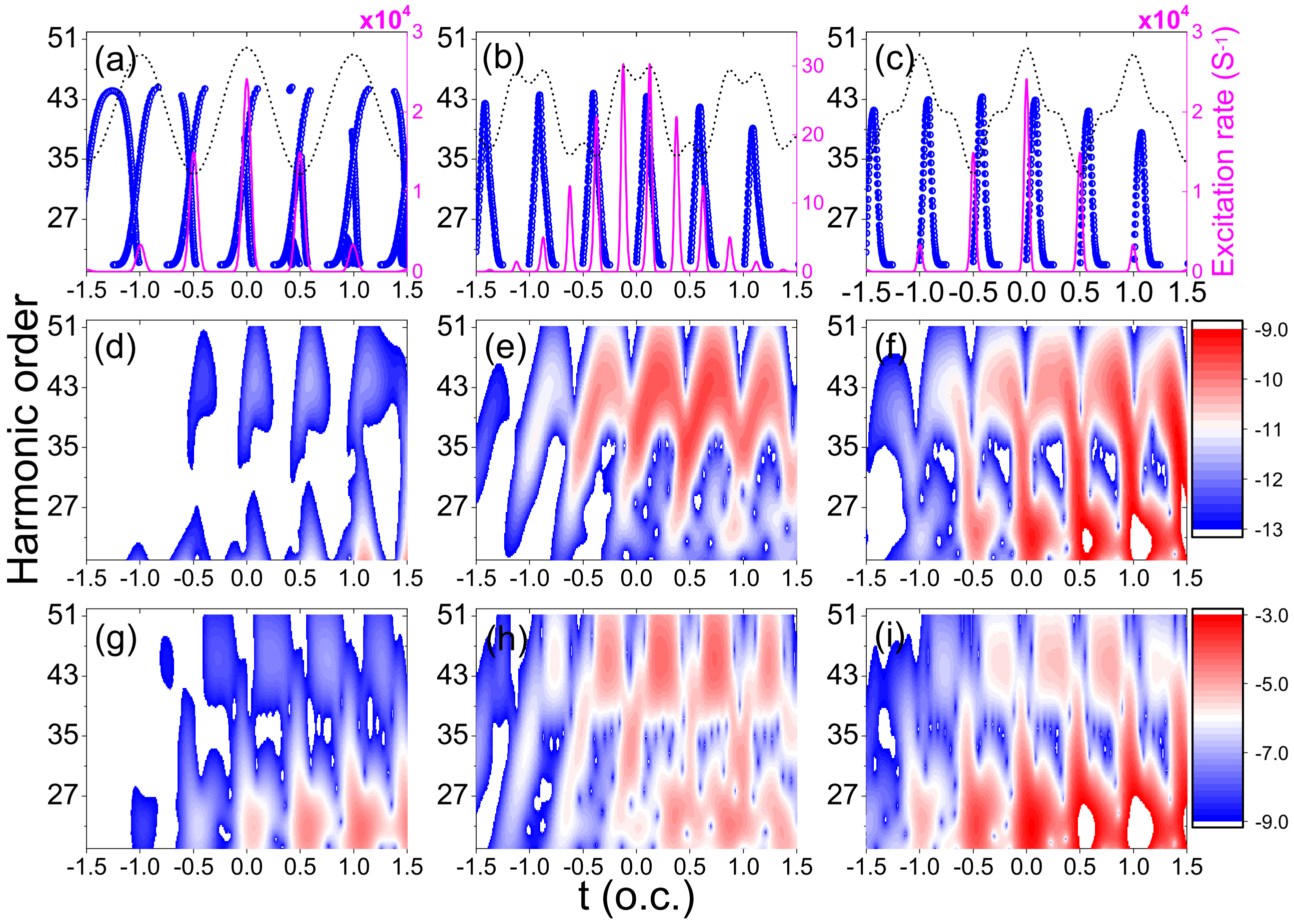

FIG. 4. (a–c) Harmonic order (blue circles), temporal excitation rates (magenta solid line), and laser temporal waveform (black dashed line) as a function of the tunneling time. (d–f) Temporal harmonic profile on the logarithm scale (the TDM is obtained from $\mathbf{k}\cdot\mathbf{p}$ theory). (g–i) Same as the middle row with the TDM calculated from DFT. (a, d, g) Solid harmonic generation driven by a single 54.17-fs 3250-nm pulse, E_0=0.004 a.u. (b, e, h) Solid harmonic generation driven by ω-3ω two-color fields with a π relative phase shift. Fundamental pulse: τ_1=54.17 fs, 3250-nm pulse, E_1=0.003 a.u.. Control pulse: τ_2=54.17 fs, 1083.33-nm pulse, E_2=0.001 a.u. (c, f, i) Same as the middle column but with zero relative phase shift. In all the calculations, the dephasing time T_2=0.5 o.c. (5.4 fs for the 3250-nm laser).

In Fig. 5, we compare the harmonic yield generated by the monochromatic field, the two-color field superposed by the second and third-harmonic control pulses. In Fig. 5(a), the laser parameters for the monochromatic field are 54.17 fs, 3250 nm, $E_0 = 0.004$ a.u. For the two-color field, the field strengths of the fundamental pulse and the third-harmonic control pulse are $E_1 = 0.003$ a.u. and $E_2 = 0.001$ a.u. ($\kappa = 0.33$). Thus the monochromatic and the two-color fields have the same total field strength.

The harmonic yield at the primary plateau region (from the 23rd harmonic to the 39th harmonic) is enhanced by nearly one order of magnitude. The tunnel excitation rates calculated by the Keldysh model [51] in Figs. 4(a) and 4(c) explain why the harmonic yield is greatly enhanced. The superposed third harmonic increases the excitation rates for the trajectories contributing to the HHG spectra.

Both the results by using the TDM from $\mathbf{k}\cdot\mathbf{p}$ theory (lines) and DFT (scatters) are plotted and the curves show a similar trend. The yield is obtained by integrating the harmonics from the 21st to 51st order in the plateau region of the HHG spectra. We find that the harmonic yield increases exponentially with the relative strength ratio. The third-harmonic control (red scatters and lines) shows better enhancement of the HHG yield than increasing the field strength of the fundamental pulse (black scatters and lines) and the second-harmonic control (blue scatters and lines).

The calculation result shows that, for interband transition in solid HHG, through superposing a weak third harmonic (with a relative intensity ratio of 0.1), the yield on the plateau region of harmonic spectra can be improved by nearly one order of magnitude. The great enhancement of harmonic yield by using the third-harmonic pulse field is similar to the experimental observation [59] and calculation [60] in the atomic HHG. The two-color field modulation can effectively improve the yield of extreme ultraviolet (EUV) sources from solid HHG.

In the following, we investigate the IAP generation by employing the two-cycle 3250-nm laser pulse superposed by a third-harmonic field. Figures 6(c) and 6(d) show the temporal harmonic profile on a logarithmic scale. Figure 6(c) shows the temporal profile driven by a 20.67-fs $E_0 = 0.003$-a.u. 3250-nm pulse superposed by its third harmonic with a relative intensity ratio of 0.1 with zero phase shift. Figure 6(d) shows the temporal harmonic profile driven by the same two-color

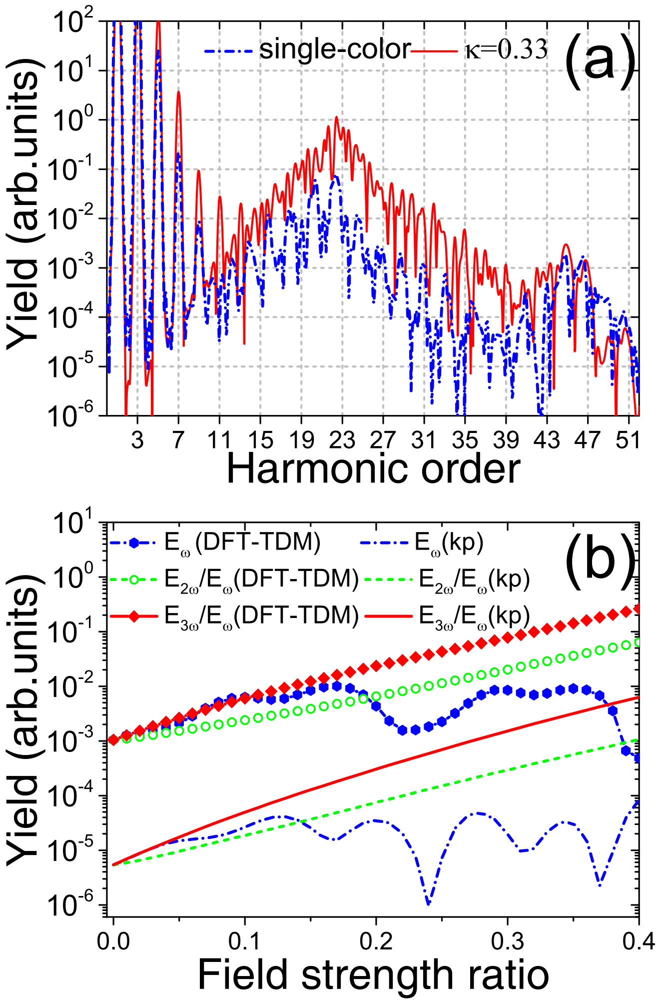

FIG. 5. (a) The harmonic spectra generated by monochromatic (blue dashed line) and two-color fields (red solid line). The monochromatic field: 54.17 fs (5 o.c.), 3250 nm, $E_0 = 0.004$ a.u. The two-color field: for the fundamental pulse, 54.17 fs (5 o.c.), 3250-nm pulse, $E_1 = 0.003$ a.u.; for the control pulse, 54.17 fs (5 o.c.), 1083.33-nm pulse, $E_2 = 0.001$ a.u. (b) The integrated yield of the plateau region of HHG spectra vs the relative field strength ratio of the control pulse. The yield is integrated in the spectral range from the 25th to 45th harmonics. The green and red lines indicate the control field with the second and third harmonics, respectively. The blue dashed line indicates the enhancement of harmonic yield by improving the field strength of the monochromatic field directly. The results by using the TDM from $\mathbf{k}\cdot\mathbf{p}$ theory (lines) and DFT (scatters) are plotted. In all the calculations, the dephasing time $T_2 =$ 0.5 o.c. (5.4 fs for the 3250-nm laser). The monochromatic field: $\tau_0 = 54.17$ fs (5 o.c.), 3250 nm, E_0 scales from 0.003 to 0.0042 a.u. For comparison, the field strength of the monochromatic field is kept the same as the two-color case, $E_0 = E_1 + E_2$. The two-color field: for the fundamental pulse, $\tau_1 = 54.17$ fs (5 o.c.), 3250-nm pulse, $E_1 = 0.003$ a.u.; for the control pulse for the ω-3ω case, $\tau_2 = 54.17$ fs (15 o.c.), 1083.33-nm pulse; for the control pulse for the $\omega - 2\omega$ case, $\tau_2 = 54.17$ fs (15 o.c.), 1625-nm pulse; E_2 scales from 0.0 to 0.0012 a.u. ($\kappa = 0.4$).

field with a π phase shift. In Figs. 6(c) and 6(d), we can see the interband harmonic emission in each half optical cycle. The harmonic bursts are mainly contributed by the short trajectories in Fig. 6(c) and long trajectories (negative chirp) in Fig. 6(d), respectively. On the same logarithmic scale, from 0.5 to 1.0 o.c., the harmonic emission in Fig. 6(c) is clearly much stronger than that in Fig. 6(d).

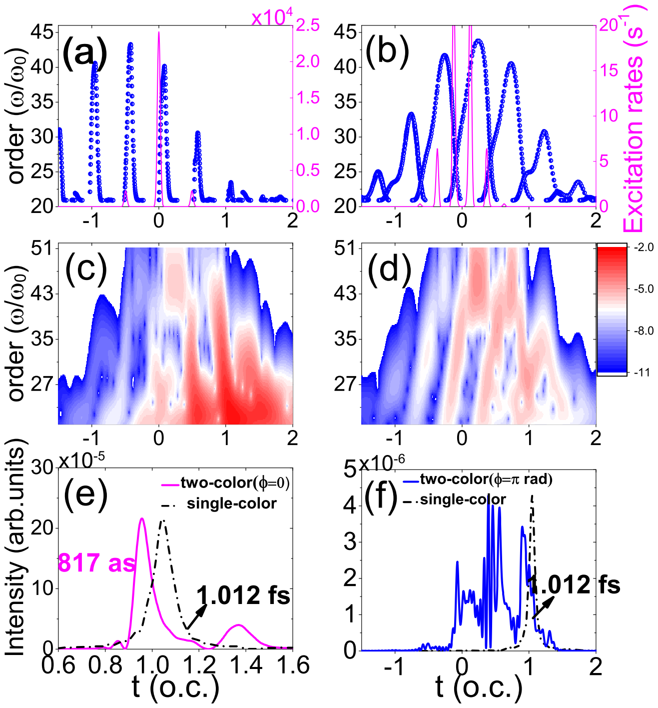

FIG. 6. (a, b) The harmonic order (blue circles) and temporal excitation rates (magenta solid line) vs the tunneling time by the two-color field with a 21.67-fs (two cycles) 3250-nm fundamental pulse and a third harmonic with a relative intensity ratio of 0.1. (c, d) The temporal high-order harmonic profile generated by the two-color field shown in the upper row. (e, f) The temporal profile of the synthesized IAP. The IAP is synthesized by inverse Fourier transforming the harmonics from the 25th to 45th order. The temporal profile of the single-color case is normalized to the same total power of the two-color case. (a, c, e) Long trajectories are selected with zero relative phase shift. (b, d, f) Short trajectories are selected with a π phase shift. In all the calculations, the dephasing time $T_2 = 0.5$ o.c. (5.4 fs for the 3250-nm laser). The monochromatic field: $\tau_0 = 21.67$ fs (two cycles), 3250 nm, $E_0 = 0.004$ a.u. The two-color field: for the fundamental pulse, $\tau_1 = 21.67$ fs, 3250-nm pulse, $E_1 = 0.003$ a.u.; for the control pulse, $\tau_2 = 54.17$ fs, 1083.33-nm pulse, $E_2 = 0.001$ a.u. For comparison, the field strength of the monochromatic field is kept the same as the two-color case, $E_0 = E_1 + E_2$.

The recollision and temporal excitation rates shown in Figs. 6(a) and 6(b) explain why the long and short trajectories are selected in Figs. 6(c) and 6(d). In Fig. 6(a), in each half optical cycle, a pair of long and short trajectories is generated. The first and second emission events can be ignored because the excitation rates are small. In the third emission event, the excitation rate peak is located at the birth time of the cutoff trajectory. Thus, the third emission event could be isolated by this tunneling gating. Besides this, the yield of this trajectory can be enhanced. Since this isolated emission occurs within a half optical cycle, the FWHM is naturally within the subfemtosecond timescale. Our simulation indicates that the quantum path selection in the interband transition is not only applicable to the few-cycle driving pulse but also works well for a multicycle driving field.

In Figs. 6(e) and 6(f), the attosecond bursts are synthesized through inverse Fourier transforming harmonic emission in the spectral range from the 25th to 45th harmonics. Compared with the IAP synthesized from the monochromatic field (black dash-dotted line), the yield of IAP is enhanced by 11.2% (magenta solid line) in Fig. 6(e). The FWHM of this IAP is 817 as. However, the two-color phase shift of π does not produce an IAP, a series of attosecond bursts are generated instead, and the intensity of generated attosecond bursts does not enhance much compared with the 1.012-fs IAP generated in the single-color case. Compared with the atomic HHG, solid HHG is expected to be a promising EUV source due to its highly orientated and dense atoms inside the crystal. Through the quantum path selection in interband transitions driven by a two-color pulse field, an IAP can be synthesized. By choosing a proper relative phase, the brightness of the IAP is expected to be enhanced greatly.

IV. CONCLUSION

The motivation of this paper is to investigate the temporal dynamic information contained in the fringe patterns of the solid high-order harmonic spectra. First, the field strength dependence curve of the 19th harmonic spectra exhibits a sharp minimum driven by a 1600-nm laser field polarized along the ΓX direction of MgO crystal. Our theoretical simulation based on the SBE confirms that this minimum comes from the coherent interferences between the short and long trajectories in interband transitions. In addition to the harmonic splitting in sapphire [43], the interference should be a phenomenon occurring in many crystals.

For the dephasing of the target material, we have tested its role. In the range of T_2 from 0.5 o.c. (2.67 fs) to 2.0 o.c. (10.6 fs), the interference minimum is robust in our simulations.

Our calculations show that the temporal dynamics of the electrons and holes inside the crystal can be modulated by controlling the laser parameters. By modulating the field strength, the quantum paths can be controlled on the attosecond timescale. In addition, by controlling the quantum path interference, a specific harmonic can be selectively strengthened or suppressed.

Second, our calculation demonstrates that the quantum path interference minimum in interband transitions has a sensitive dependence on the band structure. Since the electron wave packets accumulate phases when they move along the band, their accumulated phases record the band dispersion information. As an all-optical method, this quantum path interference minimum can be utilized to retrieve the band structure.

Third, the short or long trajectory in interband transitions can be selected by using the two-color fields with a proper phase. Moreover, our calculation illustrates that the plateau and the cutoff region of HHG spectra can be enhanced by one order of magnitude by superposing a weak third harmonic with a relative intensity ratio of 0.1.

Finally, by employing a two-cycle fundamental pulse and a weak third harmonic as a control field with an intensity ratio of 0.1, an IAP is synthesized from HHG with FWHM=817 as. Its brightness is enhanced by 11.2% compared with the IAP synthesized by the single-color field. This indicates that for the solid HHG as a potential attosecond EUV source its brightness can be further enhanced by the two-color scheme.

This quantum path interference in interband transitions and the quantum path selection by a two-color scheme have been less investigated to our knowledge. This may stimulate related experimental studies in the future.

In this paper, we also ignore the band-structure renormalization due to the laser-induced change of charge density, the electron-electron scattering, and interactions. Although DFT is accurate for the ground-state-like valence band for crystal, it does not treat excited states well. It should be noted that the calculated conduction-band dispersions from DFT may have deviations from the actual conduction band. The mesoscopic effects, nonlinear propagation inside crystals, and inhomogeneous illumination [61] may make the minimum or splitting pattern induced by the quantum path interference difficult to observe. For the experimental realization of our interference model, if we use short-wavelength lasers, control the laser focusing, and use thin samples with very high purity, the above influences might be minimized.

ACKNOWLEDGMENTS

The authors thank D. Tang, X.-Q. Wang, J.-X. Liu, A.-W. Zeng, C.-L. Xia, and M.-H. Yuan for helpful discussions. This work is supported by the National Natural Science Foundation of China (Grants No. 91850121 and No. 11674363) and the National Key Research and Development Program of China (Grant No. 2019YFA0307702).

APPENDIX A: FIRST-PRINCIPLES CALCULATIONS

To obtain the band structure and dipole information of a MgO primitive cell, we perform our first-principles calculations using the Vienna Ab Initio Simulation package (VASP) [63], which self-consistently solves the Kohn-Sham equations for eigenvalues and eigenfunctions of the periodic system. The transition dipole moments are obtained by using the post-processing program VASPKIT [64]. To describe the exchange-correlation functional, the local-density approximation is used in our calculations.

In the present paper, the full potential projector augmented wave method describes the ion-electron interactions with

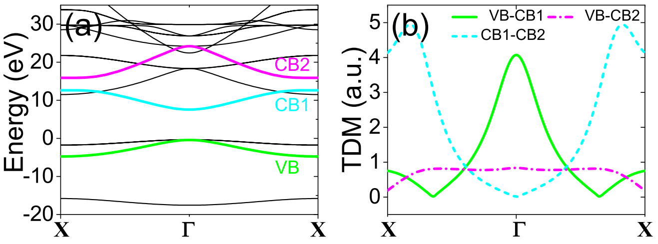

FIG. 7. (a) The band structure of the MgO primitive unit cell along the ΓX direction. (b) The modulus of the transition dipole moment between each pair of bands considered in the SBE.

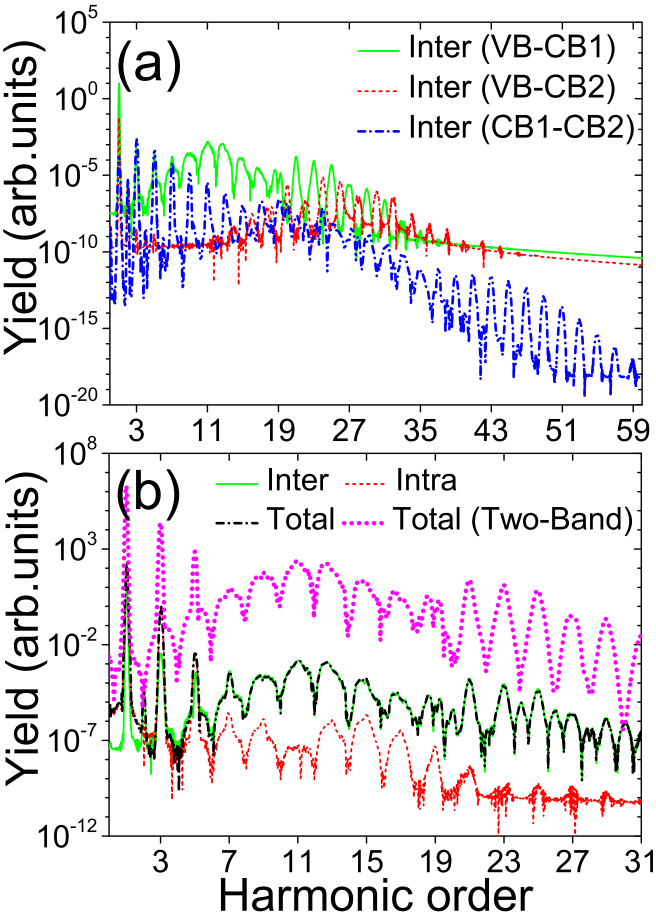

FIG. 8. Multiband effects on HHG. (a) The interband transition from each pair of bands. (b) The interband and intraband transitions, and their total contribution to HHG. A clearly splitting minimum pattern is observed from HHG spectra when high-lying band CB2 is included. It is the same as the minimum observed from the two-band model (up shifted for comparison) shown in Fig. 2(c). The laser parameters used in the simulation are the same as those in Fig. 2(c).

a plane-wave cutoff of 500 eV. In the self-consistent cycle, the Brillouin zone (BZ) is sampled by a 20 × 20 × 20 Monkhorst-Pack k-point mesh for self-consistent converged calculations for charge density and wave function.

The two-band SBE is based on the electronic band dispersion values for the MgO primitive cell from the above first-principles calculations. The obtained direct band gap $E_g = 7.99$ eV. Figure 7(a) plots the band structures. Figure 7(b) shows the modulus of the transition dipole moment between each pair of bands. CB2 in Fig. 7 is chosen according to the dominant transition probabilities between VB, CB1, and CB2 [17]. The band dispersion curves and TDM in the reciprocal space are originally computed from VASP and fitted by the Fourier series:

$$\epsilon_{\mathrm{CB}}(K_X) = \epsilon_g + \sum_{j=0}^{n} \alpha_{\mathrm{CB}}^{j} \cos(jK_X a_X), \tag{A1}$$

$$\epsilon_{\mathrm{VB}}(K_X) = \sum_{j=0}^{n} \alpha_{\mathrm{VB}}^{j} \cos(jK_X a_X), \tag{A2}$$

where a_X is the length of the lattice and K_X is the Bloch vector. The polarization direction $\widehat{E}$ of the driving laser field is along the ΓX direction with a_X=7.78 bohrs for the MgO [34–37,62] primitive cell. The SBEs are solved by the finite difference method with 250 k-space points (full BZ) along ΓX and the crystal momentum grid $\Delta k = 0.00324$ a.u.

APPENDIX B: MULTIBAND EFFECTS

To evaluate the role of the high-lying bands [65] in the HHG spectra, the three-band model which includes a high-lying band CB2 is used in the calculations. Figure 8(a) plots the interband transitions between each pair of bands in the SBE calculation. The interband transition between CB1 and CB2 has little effect on the primary plateau region of spectra. This is because the population of the higher conduction band is pumped from the first conduction band CB1 according to the step-by-step model [22,66]; therefore, the population in CB2 is much smaller than that in CB1. Its contribution to the primary plateau region and the 19th harmonic is much less than the contribution from CB1.

One may find that the primary plateau region calculated by the three-band model agrees well with the two-band model. In Fig. 8(b), a clearly splitting minimum pattern is observed at the 19th harmonic on HHG spectra when the high-lying band CB2 is included, which is the same as the minimum observed from the two-band model shown by the magenta dotted line. For the even harmonics illustrated in Fig. 8, they come from the dynamic asymmetry induced by the interference of multibands [16,66].

---

[1] A. McPherson, G. Gibson, H. Jara, U. Johann, T. S. Luk, I. A. McIntyre, K. Boyer, and C. K. Rhodes, J. Opt. Soc. Am. B **4**, 595 (1987).
[2] P. B. Corkum, Phys. Rev. Lett. **71**, 1994 (1993).
[3] M. Lewenstein, P. Balcou, M. Y. Ivanov, A. L'Huillier, and P. B. Corkum, Phys. Rev. A **49**, 2117 (1994).
[4] M. Hentschel, R. Kienberger, R. Kienberger, G. A. Reider, N. Milosevic, T. Brabec, P. Corkum, U. Heinzmann, M. Drescher, and F. Krausz, Nature (London) **414**, 509 (2001).
[5] P. M. Paul, E. S. Toma, P. Breger, G. Mullot, F. Augé, P. Balcou, H. G. Muller, and P. Agostini, Science **292**, 1689 (2001).
[6] J. Itatani, J. Levesque, D. Zeidler, H. Niikura, H. Phpin, J. C. Kieffer, P. B. Corkum, and D. M. Villeneuve, Nature (London) **432**, 867 (2004).
[7] S. Minemoto, T. Umegaki, Y. Oguchi, T. Morishita, A. T. Le, S. Watanabe, and H. Sakai, Phys. Rev. A **78**, 061402(R) (2008).
[8] H. J. Wörner, H. Niikura, J. B. Bertrand, P. B. Corkum, and D. M. Villeneuve, Phys. Rev. Lett. **102**, 103901 (2009).

[9] M. Lein, N. Hay, R. Velotta, J. P. Marangos, and P. L. Knight, Phys. Rev. Lett. **88**, 183903 (2002).
[10] M. Lein, J. Phys. B **40**, R135 (2007).
[11] H. Niikura, F. Légaré, R. Hasbani, A. D. Bandrauk, M. Ivanov, D. M. Villeneuve, and P. B. Corkum, Nature (London) **417**, 917 (2002).
[12] X. B. Bian and A. D. Bandrauk, Phys. Rev. Lett. **113**, 193901 (2014).
[13] A. H. Chin, O. G. Calderón, and J. Kono, Phys. Rev. Lett. **86**, 3292 (2001).
[14] S. Ghimire, A. D. DiChiara, E. Sistrunk, P. Agostini, L. F. DiMauro, and D. A. Reis, Nat. Phys. **7**, 138 (2011).
[15] M. Hohenleutner, F. Langer, O. Schubert, M. Knorr, U. Huttner, S. W. Koch, M. Kira, and R. Huber, Nature (London) **523**, 572 (2015).
[16] G. Ndabashimiye, S. Ghimire, M. Wu, D. A. Browne, K. J. Schafer, M. B. Gaarde, and D. A. Reis, Nature (London) **534**, 520 (2016).
[17] Y. S. You, M. Wu, Y. Yin, A. Chew, X. Ren, S. Gholam-Mirzaei, D. A. Browne, M. Chini, Z. Chang, K. J. Schafer, M. B. Gaarde, and S. Ghimire, Opt. Lett. **42**, 1816 (2017).
[18] N. Yoshikawa, T. Tamaya, and K. Tanaka, Science **356**, 736 (2017).
[19] N. Tancogne-Dejean, O. D. Mücke, F. X. Kärtner, and A. Rubio, Nat. Commun. **8**, 745 (2017).
[20] G. Vampa, T. J. Hammond, N. Thiré, B. E. Schmidt, F. Légaré, C. R. McDonald, T. Brabec, and P. B. Corkum, Nature (London) **522**, 462 (2015).
[21] G. Vampa, C. R. McDonald, G. Orlando, D. D. Klug, P. B. Corkum, and T. Brabec, Phys. Rev. Lett. **113**, 073901 (2014).
[22] T.-Y. Du and X.-B. Bian, Opt. Express **25**, 151 (2017).
[23] P. Földi, Phys. Rev. B **96**, 035112 (2017).
[24] R. E. F. Silva, F. Martín, and M. Ivanov, Phys. Rev. B **100**, 195201 (2019).
[25] X. Q. Wang, Y. Xu, X. H. Huang, and X. B. Bian, Phys. Rev. A **98**, 023427 (2018).
[26] G. Ernotte, T. J. Hammond, and M. Taucer, Phys. Rev. B **98**, 235202 (2018).
[27] T. J. Hammond, S. Monchocé, C. Zhang, G. Vampa, D. Klug, A. Y. Naumov, D. M. Villeneuve, and P. B. Corkum, Nat. Photonics **11**, 594 (2017).
[28] G. Vampa, T. J. Hammond, N. Thiré, B. E. Schmidt, F. Légaré, C. R. McDonald, T. Brabec, D. D. Klug, and P. B. Corkum, Phys. Rev. Lett. **115**, 193603 (2015).
[29] Y. S. You, D. A. Reis, and S. Ghimire, Nat. Phys. **13**, 345 (2017).
[30] N. Saito, P. Xia, F. Lu, T. Kanai, J. Itatani, and N. Ishii, Optica **4**, 1333 (2017).
[31] Z.-Y. Chen and R. Qin, Opt. Express **27**, 3761 (2019).
[32] Z. Guan, X. X. Zhou, and X. B. Bian, Phys. Rev. A **93**, 033852 (2016).
[33] T. Y. Du, D. Tang, and X. B. Bian, Phys. Rev. A **98**, 063416 (2018).
[34] T. Y. Du, D. Tang, X. H. Huang, and X. B. Bian, Phys. Rev. A **97**, 043413 (2018).
[35] F. Navarrete, M. F. Ciappina, and U. Thumm, Phys. Rev. A **100**, 033405 (2019).
[36] X. H. Song, R. X. Zuo, S. D. Yang, P. C. Li, T. Meier, and W. F. Yang, Opt. Express **27**, 2225 (2019).
[37] R.-X. Zuo, X.-H. Song, X.-W. Liu, S.-D. Yang, and W.-F. Yang, Chinese Phys. B **28**, 094208 (2019).
[38] O. Neufeld, D. Podolsky, and O. Cohen, Nat. Comm. **10**, 405 (2019).
[39] A. Zaïr, M. Holler, A. Guandalini, F. Schapper, J. Biegert, L. Gallmann, U. Keller, A. S. Wyatt, A. Monmayrant, I. A. Walmsley, E. Cormier, T. Auguste, J. P. Caumes, and P. Salières, Phys. Rev. Lett. **100**, 143902 (2008).
[40] T. Auguste, P. Salières, A. S. Wyatt, A. Monmayrant, I. A. Walmsley, E. Cormier, A. Zair, M. Holler, A. Guandalini, F. Schapper, J. Biegert, L. Gallmann, and U. Keller, Phys. Rev. A **80**, 033817 (2009).
[41] C. M. Heyl, J. Güdde, U. Höfer, and A. L'Huillier, Phys. Rev. Lett. **107**, 033903 (2011).
[42] I. K. Kominis, G. Kolliopoulos, D. Charalambidis, and P. Tzallas, Phys. Rev. A **89**, 063827 (2014).
[43] Y. W. Kim, T.-J. Shao, H. Kim, S. Han, S. Kim, M. Ciappina, X.-B. Bian, and S.-W. Kim, ACS Photonics **6**, 851 (2019).
[44] B. K. McFarland, J. P. Farrell, P. H. Bucksbaum, and M. Gühr, Science **322**, 1232 (2008).
[45] O. Smirnova, Y. Mairesse, S. Patchkovskii, N. Dudovich, D. Villeneuve, P. Corkum, and M. Y. Ivanov, Nature (London) **460**, 972 (2009).
[46] L.-J. Lü and X.-B. Bian, Phys. Rev. B **100**, 214312 (2019).
[47] M. S. Mrudul, A. Pattanayak, M. Ivanov, and G. Dixit, Phys. Rev. A **100**, 043420 (2019).
[48] G. Vampa, C. R. McDonald, G. Orlando, P. B. Corkum, and T. Brabec, Phys. Rev. B **91**, 064302 (2015).
[49] C. R. McDonald, G. Vampa, P. B. Corkum, and T. Brabec, Phys. Rev. A **92**, 033845 (2015).
[50] C. Yu, X. Zhang, S. Jiang, X. Cao, G. Yuan, T. Wu, L. Bai, and R. Lu, Phys. Rev. A **94**, 013846 (2016).
[51] L. V. Keldysh, J. Exp. Theor. Phys. **47**, 1945 (1964) [Sov. Phys. JETP **20**, 1307 (1965)].
[52] F. Brizuela, C. M. Heyl, P. Rudawski, D. Kroon, L. Rading, J. M. Dahlström, J. Mauritsson, P. Johnsson, C. L. Arnold, and A. L'Huillier, Sci. Rep. **3**, 1410 (2013).
[53] J.-B. Li, X. Zhang, S.-J. Yue, H.-M. Wu, B.-T. Hu, and H.-C. Du, Opt. Express **25**, 18603 (2017).
[54] S. Jiang, H. Wei, J. Chen, C. Yu, R. Lu, and C. D. Lin, Phys. Rev. A **96**, 053850 (2017).
[55] J. Li, X. Zhang, S. Fu, Y. Feng, B. Hu, and H. Du, Phys. Rev. A **100**, 043404 (2019).
[56] Z. Zeng, Y. Cheng, X. Song, R. Li, and Z. Xu, Phys. Rev. Lett. **98**, 203901 (2007).
[57] X. Song, Z. Zeng, Y. Fu, B. Cai, R. Li, Y. Cheng, and Z. Xu, Phys. Rev. A **76**, 043830 (2007).
[58] N. Ishii, A. Kosuge, T. Hayashi, T. Kanai, J. Itatani, S. Adachi, and S. Watanabe, Opt. Express **16**, 20876 (2008).
[59] S. Watanabe, K. Kondo, Y. Nabekawa, A. Sagisaka, and Y. Kobayashi, Phys. Rev. Lett. **73**, 2692 (1994).
[60] C. Jin, G. Wang, H. Wei, A. T. Le, and C. D. Lin, Nat. Commun. **5**, 4003 (2014).
[61] I. Floss, C. Lemell, G. Wachter, V. Smejkal, S. A. Sato, X. M. Tong, K. Yabana, and J. Burgdörfer, Phys. Rev. A **97**, 011401(R) (2018).
[62] S. Iacobucci, F. Offi, P. Torelli, and L. Petaccia, J. Electron Spectros. Relat. Phenomena **233**, 1 (2019).
[63] G. Kresse and J. Hafner, Phys. Rev. B **47**, R558 (1993).

[64] V. Wang, N. Xu, J. C. Liu, G. Tang, and W. T. Geng, VASPKIT: A Pre- and Post-Processing Program for VASP code, arXiv:1908.08269 (2019).

[65] A. J. Uzan, G. Orenstein, A. Jiménez-Galán, C. McDonald, R. E. F Silva, B. D. Bruner, N. D. Klimkin, V. Blanchet, T. Arusi-parpar, M. Krüger, A. N. Rubtsov, O. Smirnova, M. Ivanov, B. Yan, T. Brabec, and N. Dudovich, arXiv:1812.02498 (2018).

[66] G.-R. Jia, X.-H. Huang, and X.-B. Bian, Opt. Express **25**, 23654 (2017).